Stress mapping of undamaged, strained, and failed regions of bone using Raman spectroscopy

Kathryn A. Dooley
University of Michigan
Department of Chemistry
930 North University Avenue
Ann Arbor, Michigan 48109

Jordan McCormack
David P. Fyhrie
University of California, Davis
Lawrence J. Ellison Musculoskeletal Research Center
4860 Y Street
Sacramento, California 95817

Michael D. Morris
University of Michigan
Department of Chemistry
930 North University Avenue
Ann Arbor, Michigan 48109
E-mail: mdmorris@umich.edu

Abstract. Stress differences via spectral shifts that arise among failed, strained, and undamaged regions of bone can be determined using Raman spectroscopy and double-notch specimens. A double-notch specimen is a model in which the early stages of fracture can be examined. At four-point bending, fracture occurs at one of the notches. Tissue near each notch is representative of bone in a state either directly before or after bone failure. Raman images are acquired among three regions: control, strained (root of unbroken notch), and failed (root of fractured notch). The center of gravities (CGs), a way to monitor wavenumber shifts, of the phosphate v_1 band are calculated. A PO_4^{-3} v_1 band shift most likely corresponds to a change in spacing between phosphate cations and anions. This spectral shift is converted into stress values using the dv/dP coefficient, determined by applying known pressures/stresses and measuring the change in position of the PO_4^{-3} v_1 band. In comparison to control regions, the residual stress in strained and failed regions is significantly higher ($p=0.0425$ and $p=0.0169$, respectively). In strained regions, residual stress is concentrated near the corners of the unbroken notch, whereas in failed regions the high stresses are confined near the edge of the fracture.
 [DOI: 10.1117/1.3184435]

Keywords: Raman spectroscopy; bone; imaging; double-notch; bone mechanics.

Paper 08173RR received May 29, 2008; revised manuscript received Feb. 24, 2009; accepted for publication Jun. 2, 2009; published online Jul. 31, 2009. This paper is a revision of a paper presented at the SPIE Conference on Biomedical Optical Spectroscopy, January 2008, San Jose, California. The paper presented there appears (unrefereed) in SPIE Proceedings Vol. 6853

1 Introduction

Vibrational spectroscopy has been used to monitor the response of bone to external stress. One common spectroscopic response to external stress is a wavenumber shift in one or more of the spectral bands. For example, in high-pressure studies of calcium hydroxyapatite and other inorganic minerals similar to bone mineral,[1–4] the vibrational bands associated with the phosphate groups were shown to exhibit strain-dependent shifts. Subsequent high-pressure x-ray diffraction and Raman spectroscopic studies by Comodi et al. found that the phosphate v_1 band shift in fluorapatite was mainly due to a change in the cation/anion spacing of phosphate.[5,6] Similar effects in bone have been seen in our laboratory, including high-pressure Raman studies[7] and ongoing nuclear magnetic resonance spectroscopy (NMR) experiments.[8]

In studies on bone, the mineral component has been examined in microdamaged,[9] fractured,[10] and nanoindented[11] regions. Researchers have observed a shift in the PO_4^{-3} v_1 symmetric stretch, the most intense band in the bone spectrum. In microdamaged and fractured regions, an additional mineral factor was present, whose PO_4^{-3} v_1 band corresponded to a higher wavenumber (963 and 965 cm^{-1}, respectively) than the carbonated hydroxyapatite typically found in bone ($\sim$959 cm^{-1}). In the nanoindentation study, a PO_4^{-3} v_1 band shift occurred in the middle of the indent where compression had occurred. A shift was not observed in the control region outside the indent, indicating that the shift was an effect of damage, and not a cause of it.

Pezzotti and Sakakura have taken advantage of this phenomenon and monitored a shift in the PO_4^{-3} v_1 band during fracture propagation of bovine cortical bone.[12–14] Quantitative stress fields were calculated and Raman stress maps were generated, allowing toughening mechanisms such as microcracking to be visualized. In subsequent studies, the PO_4^{-3} v_1 band shift was monitored in murine bone during physiological loading and observed to change.[15] On nanoindented teeth, Raman images were generated mapping this wavenumber shift.[16] The results of these studies suggest bone mineral plays a dynamic role in the response to external stress.

Because the mineral band position is sensitive to stress, we wanted to monitor the mineral response in a bone model where understanding stress distributions would be important, such as in a fracture model. Nalla, Kinney, and Ritchie introduced into the biomechanics literature the double-notch specimen, a model in which the early stages of fracture can be examined.[17] The specimens are rectangular beams of bone

Address all correspondence to: Michael D. Morris, University of Michigan, Department of Chemistry, 930 N. University Ave., Ann Arbor, MI 48109; Tel: 1-734-764-7360; Fax: 1-734-764-0477; E-mail: mdmorris@umich.edu

1083-3668/2009/14(4)/044018/8/$25.00

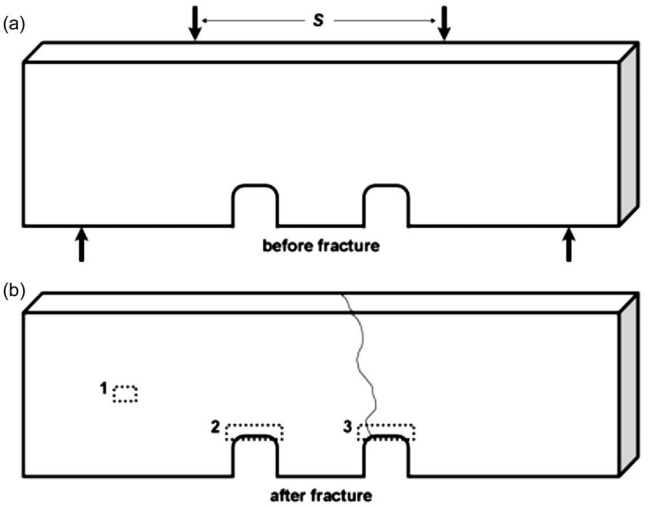

Fig. 1 Double-notch specimens. (a) Specimen geometry. (b) At four-point bending, the bone fractured at one of the notches. The dashed lines indicate the three regions where Raman images were acquired: 1. control, 2. non-fractured, and 3. fractured regions, respectively.

that have similar rounded notches milled equidistant from each end. In four-point bend tests, maximum strains occur at the roots of the notches, and eventually the bone fractures at one of the notches. Because both notches experience the same bending moment, when one notch breaks, the other remains "frozen" in the state directly preceding fracture.

The objective of this preliminary study was to determine stress distributions in the double-notch specimen using Raman imaging. We acquire spectra around the roots of unbroken and fractured notches and monitor stress via spectral shifts in the PO_4^{-3} v_1 band. The resulting Raman images map the stress distribution.

2 Materials and Methods

2.1 *Specimen Preparation*

Fresh-frozen equine third metacarpals (Mc-3) from three female thoroughbreds were used. One horse died of a fracture of the left forelimb fetlock, and the cause of death of the other two horses was unknown. Specimens were milled to approximate dimensions of 2 mm (width) $\times$ 2 mm (thickness) $\times$ 21 mm (length). The geometry of the specimens is shown in Fig. 1. Specimen length corresponded to the long axis of the bone. Rounded notches (depth $\sim$0.6 to 0.7 mm) were created using a 0.75-mm dental cutting disk (SummaDisk, Shofu Corporation) mounted on a CNC machine. The depths of both notches were made as similar as possible to ensure comparable stress-strain fields at the notch tips. Symmetric four-point bending tests (inner loading span $S \sim 5$ mm) were conducted on the double-notch specimens. The specimens were loaded at 0.01 mm/s using an EnduraTec ELF 3200 testing machine (BOSE Corporation, ElectroForce Systems Group, Eden Prairie, Minnesota). The bone was in tension on the side where the notches were located. The specimens remained hydrated throughout the preparation and testing procedures. Specimens were stored at -80 °C until Raman images were acquired.

2.2 *Raman Imaging*

A locally constructed Raman microprobe, described previously,[11] with a line-focused laser beam was used to image the double-notch specimens. Briefly, a $20\times/0.75$ NA objective (S Fluor, Nikon Instruments, Melville, New York) focused a 400-mW 785-nm diode laser (Invictus, Kaiser Optical Systems, Incorporated, Ann Arbor, Michigan) onto the specimen. Raman scatter was collected through the same objective and focused into a NIR-optimized spectrograph (HoloSpec f/1.8, Kaiser Optical Systems, Incorporated) equipped with a 25-μm slit to provide spectral resolution of 3 to 4 cm^{-1}. The detector was a thermoelectrically cooled, back-illuminated, deep-depletion charge-coupled device (CCD) camera (DU401-BR-DD, Andor Technology, South Windsor, Connecticut) operating at -75 °C. Hyperspectral images were acquired through the use of either a scanning mirror or motorized translation stage integrated with the microscope. For some specimens, images were acquired by scanning the line-focused laser across a stationary specimen using a single-axis galvanometer scanning mirror (6240H, Cambridge Technology, Incorporated, Lexington, Massachusetts). The field of view of the objective was smaller than the area to be imaged. Because of this, after mirror scanning over a region of 50 μm on the stationary specimen, the specimen was manually translated 50 μm, and the process repeated. Mirror movement and data acquisition were controlled via LabVIEW 7.1 (National Instruments, Austin, Texas) software. The line focus enabled the simultaneous collection of spectra for each row of pixels on the CCD detector. Spectra collected along a line in this way are called a transect. Transects were acquired using an integration time of 60 s and 3.125-μm steps. The laser power at the specimen was $\sim$105 mW. As a matter of convenience, the scanning mirror system was replaced by a motorized translation stage (H101A Proscan II, Prior Scientific, Incorporated, Rockland, Massachusetts). Hyperspectral images taken after this modification were then acquired by translating the specimen beneath the objective. Transects were acquired using an integration time of 60 s and 6.25-μm steps, and the laser power at the specimen was $\sim$170 mW. The dashed boxes labeled as 1, 2, or 3 in Fig. 1 indicate the approximate areas where images were collected. Box 1 is the undamaged area (control region), box 2 is the nonfractured notch (strained region), and box 3 is the fractured notch (failed region). During all Raman measurements, specimens were kept hydrated in phosphate buffered saline (PBS) buffer. To determine the spectral effect of protease inhibitor (Protease Inhibitor Cocktail P8340, Sigma-Aldrich, Saint Louis, Missouri), it was added to the buffer used for specimen 2.

2.3 *Data Analysis*

All data reduction was performed in MATLAB (The Mathworks, Incorporated, Natick, Massachusetts) using vendor-supplied and locally written scripts. Preprocessing included wavenumber calibration, correction for the curvature of spectral bands caused by the large gathering angle of the spectrograph, removal of noise spikes, subtraction of dark current, and correction for the wavelength response of the CCD. Data processing was only carried out in the spectral region of interest (750 to 1750 cm^{-1}), and only on pixel rows in the

middle of the CCD detector. Rows at the edges of the CCD were not processed because they did not contain spectroscopic data. An iterative baselining procedure was used to remove the background fluorescence.[18] For images taken with the scanning mirror, each 50-μm section was processed individually. The sections were then concatenated to create the final image that spanned the region either of the unbroken notch, failed notch, or control region. Phosphate center of gravities (CGs) were calculated over the range of 930 to 980 cm^{-1}, which included the PO_4^{-3} v_1 band at ~959 cm^{-1} and a prominent shoulder band at ~945 cm^{-1}. Below is the CG equation used:

$$\frac{\Sigma_{930\ cm^{-1}}^{980\ cm^{-1}}(I \times v)}{\Sigma_{930\ cm^{-1}}^{980\ cm^{-1}} I}, \tag{1}$$

where I is the intensity in counts at each specified wavenumber and v is the wavenumber value. The shift in the PO_4^{-3} v_1 CG (Δv) was determined by calculating the difference between the CG at a particular point and the average CG of the control region for that beam [Eq. (2)].

$$\Delta v = \mathrm{CG} - \mathrm{mean}(\mathrm{CG}_{\mathrm{control\ region}}). \tag{2}$$

Stresses were then calculated using the following equation:

$$\mathrm{stress} = \Delta v/(dv/dP), \tag{3}$$

where dv/dP is a coefficient representing the average change in position of the PO_4^{-3} v_1 band per unit pressure. The bovine cortical bone value of ~2.5 cm^{-1}/GPa measured by Pezzotti under four-point bending was used.[14] Finally, the effect of region (control, strain, fail) was tested with repeated measures of analysis of variance (ANOVA) using a significance value of 0.05 (SAS 9.1.3., SAS Institute, Incorporated, Cary, North Carolina).

3 Results

A representative Raman spectrum of bone is shown in Fig. 2. The most intense band in the bone spectrum is phosphate v_1, which is indicative of carbonated hydroxyapatite, and its position is sensitive to the mineral environment. The inset of the figure shows the non-Gaussian shape of the PO_4^{-3} v_1 band, with the CG labeled.

In this preliminary study, three bone specimens were imaged. Raman images taken on beam 1 from an undamaged region and at the base of the unbroken and fractured notch are shown in Fig. 3. It is important to note that all of these Raman images are maps of the stress calculated using Eq. (3). All the images for this beam are on the same color scale, and the x and y axes are in microns, where the y axis corresponds to the length of the laser line. The average stress value in the control region [Fig. 3(a)] was 0.004 MPa. The Raman image of the unbroken notch is shown in Fig. 3(b), along with a superimposed outline of the notch edge (x~30 to 360 μm) to visualize where certain features of the notch appear. In the corresponding microscope image, the central black box denotes the imaged region and the tickmarks in the box represent every 100 μm. The Raman image of the unbroken notch had higher stress, with the highest stress being concentrated at

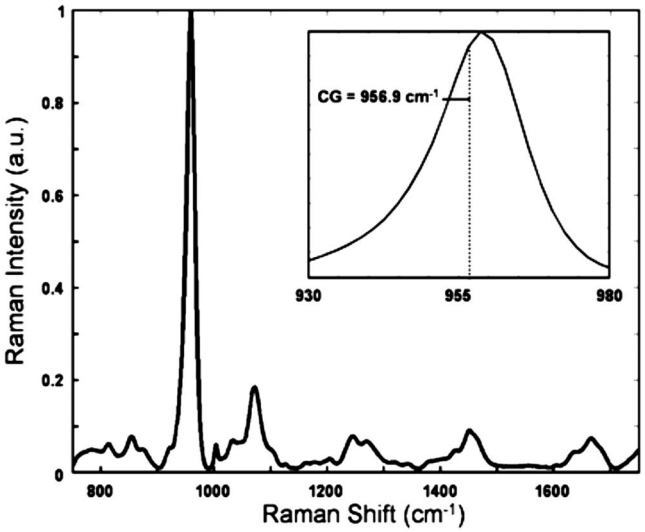

Fig. 2 Representative Raman spectrum of bone. The phosphate v_1 peak is centered at ~959 cm^{-1}. The non-Gaussian shape of this band is shown in the inset, and its center of gravity is 956.9 cm^{-1}.

the corners of the notch. At each of the unbroken notches, an average stress value was calculated from a 50×50-μm area above each corner, indicated by the dashed lines in Figs. 3(b), 4(b), and 5(b). The averages from all specimens and regions are compiled in Table 1. At the left and right corners of beam 1, the average stress values were 140.1 and 127.0 MPa. The stress propagated ~100 μm away from the notch edge. For the fractured notch [Fig. 3(c)], the edge of the notch and beginning of the fracture are located in the lower left-hand corner of the image. The outline from x~100 to 250 μm indicates the edge of the notch. The outline from 0 to 100 μm designates the edge of the fracture; the bone fractured at ~100 μm in the image and propagated off to the left. At the failed notches, average stress values were calculated from a 25×25-μm area near the edges of the fracture [these ROIs are shown in Figs. 3(c), 4(c), and 5(c)]. For beam 1, regions of higher stress (137.1 MPa) were only observed near the edge of the fracture and propagated ~50 μm away (from y~40 to 90 μm).

For beam 2 (Fig. 4), the average value in the control region was −0.01 MPa. For the nonfractured notch of beam 2, a stress pattern similar to the nonfractured notch of beam 1 was observed. The corners of the unbroken notch were right below x~200 and ~600 μm in the image. Average stresses of 81.0 MPa (left) and 162.2 (right) were seen at the very edge of these corners. Above the left corner, a stress of ~90 MPa extended ~100 μm away from the edge of the notch. At the right corner, a similar pattern was observed, except a larger magnitude stress extended into the tissue. For the fractured notch of beam 2, the fracture was located from x~100 to 400 μm and extended along the entire y axis. The regions of greatest stress were located near the left (234.3 MPa) and right (197.8 MPa) edges of the fracture. Also, a region of higher stress was located from x~850 to 900 μm, near the bottom of the image. It can be seen in Fig. 4 that the hardware change of replacing the scanning mirror with the motorized stage had a beneficial effect on

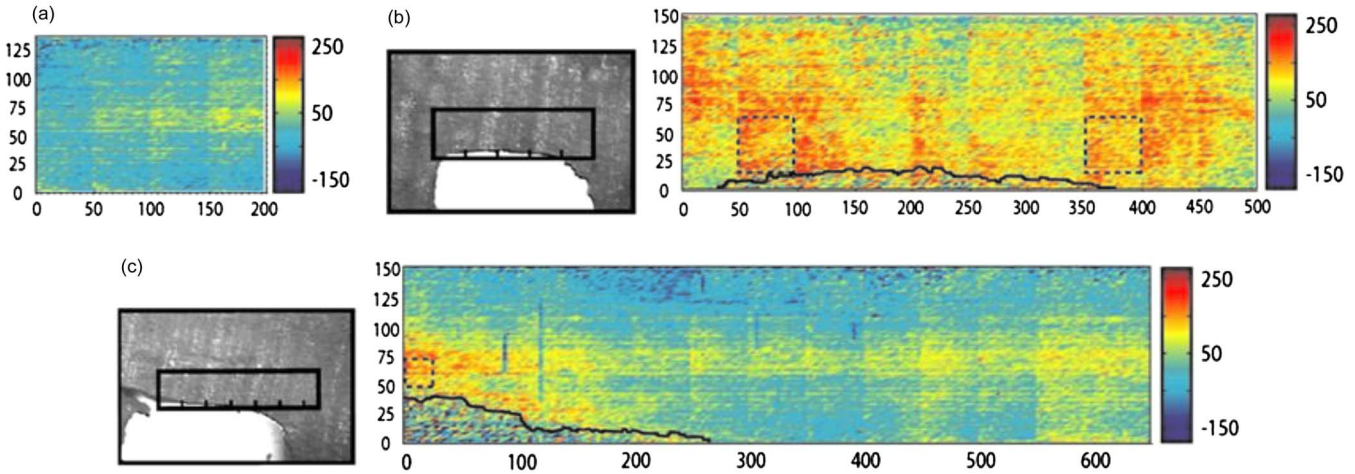

Fig. 3 Raman images of stress for specimen 1. The *x* and *y* axes are in microns, and the color bar range for all images=(−184 to 276 MPa). (a) The average stress value in the control region was 0.004 MPa. [area=0.027 mm^2]. (b) Higher stresses were concentrated at the corners of the unbroken notch, represented by the dashed boxes. The average stress values in those regions were 140.1 and 127.0 MPa. The outline at the bottom of the image was the edge of the notch. [area=0.075 mm^2]. (c) Higher stresses were observed at the edge of the fracture (137.1 MPa in the dashed region). The outline from $x\sim0$ to 100 μm was the edge of the fracture, and from $x\sim100$ to 250 μm was the edge of the notch. The subtle vertical lines visible every 50 μm were because the scanning mirror dictated images be taken in 50-μm sections, whereas the horizontal striations were due to imperfect flat-field correction [area=0.098 mm^2]. (Color online only.)

image quality; images taken with the motorized stage (i.e., Fig. 4) are "seamless," whereas images taken with the scanning mirror (i.e., Figs. 3 and 5) usually show a "seam" every 50 μm, the increment at which the specimens were manually translated.

For beam 3 (Fig. 5), the stress pattern was different from those of the previous two specimens. The average stress value in the control region was −0.01 MPa. Unlike beams 1 and 2, the stressed regions at the unbroken notch were not really focused at the corners, but instead propagated across the notch (x=0 to 500 μm) in the center of the image ($y\sim40$ to 110 μm). In this large region, the average stress value was 57.2 MPa. However, at the left and right notch corners, the average stress was 15.1 and 26.6 MPa, respectively. For the fractured notch, the fracture was in the middle of the image. In the designated region on the left side of the fracture, the average stress value was 13.2 MPa. On the right side, the average value was 43.2 MPa. Other regions of higher stress existed across the center of the image, but this was not different from the unbroken notch.

Repeated measures of ANOVA were used to test for any differences in stress values among regions (control, strain, fail). A repeated measures design was used because the three regions were imaged in each specimen. In each region, the average stress values were calculated over the two ROIs indicated on the stress maps, and these measurements were treated as an independent replicate. For the control regions, the two average stress values were calculated by splitting the image in half at x=100 μm and averaging over the first 100 μm for the first subregion and the last 100 μm for the

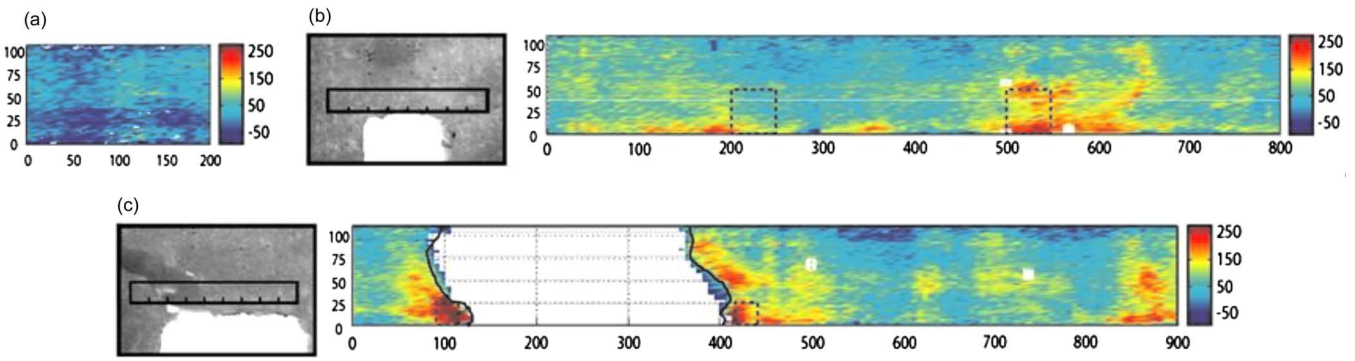

Fig. 4 Raman images of stress for specimen 2. The x and y axes are in microns, and the color bar range for all images=(−92 to 276 MPa). (a) The average stress value in the control region was −0.01 MPa [area=0.021 mm^2]. (b) Higher stresses were concentrated at the corners of the unbroken notch with the average stress values being 81.0 and 162.2 MPa. The corners of the notch were just below the Raman image, near $x\sim200$ μm and $x\sim600$ μm [area=0.088 mm^2]. (c) Higher stresses were observed at both the left (234.3 MPa) and right (197.8 MPa) edges of the fracture. The fracture was located from $x\sim100$ to 400 μm in the image. A region of higher stress was also located in the lower right-hand corner of the image, above the right corner of the notch. For the images in (b) and (c), the white spaces resulted from removal of data. For all images, imperfect flat-field correction led to striations in the horizontal direction [area=0.099 mm^2]. (Color online only.)

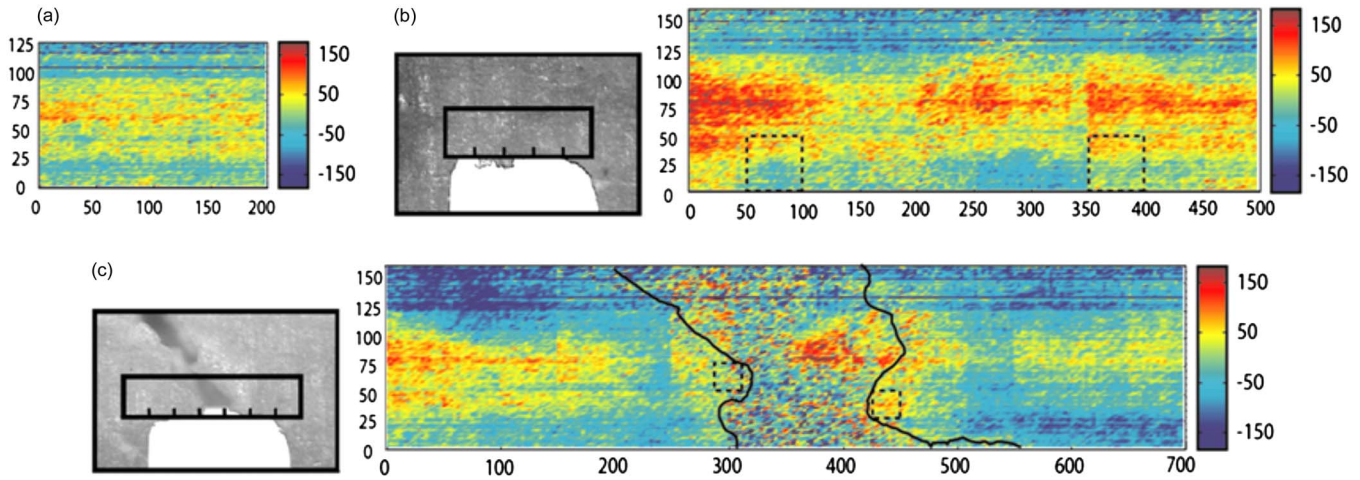

Fig. 5 Raman images of stress for specimen 3. The *x* and *y* axes are in microns, and the color bar range for all images=(−184 to 184 MPa). (a) The average stress value in the control region was −0.01 MPa [area=0.025 mm^2]. (b) Rather than being concentrated at the corners of the unbroken notch, stress propagated across the notch [area=0.083 mm^2]. (c) The bone fractured in the middle of the notch. The stresses near the left and right fracture edge were 13.2 and 43.2 MPa, respectively. Horizontal striations were due to imperfect flat-field correction [area=0.116 mm^2]. (Color online only.)

second subregion. Treating the region as the repeated factor, a significant difference in stress values was found ($p=0.0166$). Using the Tukey-Kramer *post-hoc* analysis, we found that the stress values in the control region were significantly smaller than those in the strain ($p=0.0425$) and fail regions ($p=0.0169$). Stress values did not differ significantly between the strain and fail regions ($p=0.4256$).

Because the stress patterns were different for specimen 3, a one-way ANOVA was used to detect differences among specimens, which was the between-subjects factor. A significant difference was detected ($p<0.0001$), and the Tukey-Kramer post-hoc analysis found that specimen 3 had significantly lower stress values than specimens 1 ($p=0.0003$) and 2 ($p<0.0001$).

4 Discussion

It can be seen in Fig. 2 that the shape of the PO_4^{-3} v_1 band is non-Gaussian because of unresolved shoulder bands that correspond to other phosphate environments. Thus, the CG of the PO_4^{-3} v_1 band is a useful way to gather information about different mineral environments present via changes in intensity or position of these shoulder bands. Any changes in shoulder bands are overlooked if only the peak center is examined.

Shifts in the PO_4^{-3} v_1 CG were converted into stress values using a conversion factor of 2.5 cm^{-1}/GPa. This term represents the expected wavenumber shift of the PO_4^{-3} v_1 band, and allows for the calculation of unknown stress fields in the mineral phase. It was determined by loading bovine cortical bone under four-point bending, the same type of loading used for the double-notch specimens. This value is similar to the 2.47 cm^{-1}/GPa calculated for hydroxyapatite.[19] The observed spectral shift was mainly due to a change in the spacing between the cations and anions of phosphate (a reversible effect), and a permanent change like distortion (changing bond lengths relative to one another) was far less likely. For example, Comodi et al. found very little change in the P-O bond lengths of phosphate, even when applying 4.72 GPa.[5]

Table 1 Average stress values and standard deviations for all regions. The units are MPa, and the control, strain, and failed regions are denoted by C, S, and F, respectively.

	Spec.	C Side 1	C Side 2	S L corner	S R corner	F L side	F R side
Stress	1	−7.0	7.1	140.1	127.0	NA	137.1
St dev		40.3	43.1	52.0	40.3		38.3
Stress	2	−10.1	9.5	81.0	162.2	234.3	197.8
St dev		38.1	40.4	37.9	43.4	72.3	63.4
Stress	3	0.4	−0.5	15.1	26.6	13.2	43.2
St dev		55.6	51.9	46.3	36.8	60.6	37.0

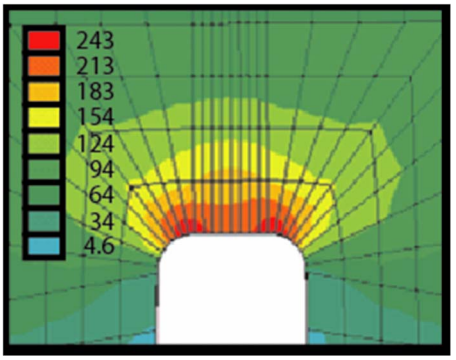

Fig. 6 Stress profile generated from a finite element model of the double-notch four-point bending specimen. The models were linear elastic and had homogeneous properties such as modulus. The S_{11} stress component is plotted, and the model shows that the stress is most concentrated near both corners of the notch, with predicted stresses of approximately 210 to 240 MPa. The units of the color scale are MPa. (Color online only.)

This pressure is far greater than that needed to fracture equine third metacarpals in four-point bending (bending strength $=227\pm27$ MPa).[20] Hence, it is very likely that the PO_4^{-3} v_1 band shift is entirely due to changes that occur in spacing between the ions of phosphate.

The region near the unbroken notch corresponded to bone in a state directly preceding fracture. The most commonly observed pattern was a higher stress concentrated above the corners of the notch. This existence of residual stress suggested that the tissue remained in a loaded state. The residual stress formed a "U" or "V" pattern, with the greatest stress being located near the notch corners, and the vertex or least stressed region being located close to the center of the notch. This pattern is consistent with the stress profile generated from a finite element model of the double-notch four-point bending specimen (Fig. 6). The S_{11} stress component is plotted, which is the direction along the length of the beam. The model shows the stress is most concentrated near both corners of the notch, with predicted stresses of approximately 230 MPa. For beams 1 and 2 [Fig. 3(b) and 4(b)], the stress in these V-shaped regions was ~134 MPa (average of the two ROIs) for beam 1 and ~122 MPa (average of the two ROIs) for beam 2, which were significantly different from the control regions. The average values we calculate are less than the bending strength (227 ± 27 MPa) but greater than the yield stress (110 ± 27 MPa) for equine third metacarpals.[20] Some likely reasons that the average values are lower than the bending strength and predicted stresses of the model are because: 1. the dv/dP coefficient was not calculated for the equine bone samples, but estimated from the dv/dP coefficient for bovine bone: and 2. The mineral is deposited in and around the matrix and its distribution is not homogeneous. This distribution probably contributes to the stripe-like morphology seen in the images, where points of high stress and low stress exist side by side. This is similar to the effect that Pezzotti has observed.[12,14] If the individual data points (rather than the averages) in these ROIs are examined, it can be seen that numerous individual points do experience stresses of over 200 MPa.

In examination of images of unbroken notches, care must be exercised in interpretation. For beam 1, the notch was located along the bottom edge of the Raman image from about 30 to 360 μm. In this region, <20 μm of the laser line was focused in the notch and not on bone. However, a bone signal was still detected even though the boundary of the notch appeared to be a sharp edge in the corresponding microscope image. The peak response of the video camera was lower than 700 nm, which minimized scattering effects in the microscope image. The near-infrared (NIR) excitation light used to generate the Raman images penetrated farther into the tissue, and the scattering response of the signal was emphasized. The nonsharp boundary in the Raman image was mainly because NIR light is multiply scattered in bone.[21] Thus, the boundary of the notch seen with visible light (microscope image) is sharper and more distinct than the boundary seen with near-infrared light (Raman image). The excitation (and Raman-generated) light propagates through the depth of the specimen, and Raman light is remitted not only from the surface of the bone, but also deeper along the notch edge. Hence, even though part of the laser beam was focused in the notch and not directly over bone, bone spectra could still be collected with our objective, albeit at a lower absolute signal and lower signal-to-noise ratio. Even in regions where the entire length of the laser line was focused on bone, Raman light that originated from deeper layers was collected. However, this out-of-focus light had a lower intensity and lower signal-to-noise ratio than the in-focus light at the surface of the bone. To exclude this effect, the system would need to be confocal, but this would result in reduced signal.

The stress pattern near the unbroken notches was different from the pattern near the fractured notches, even though both regions nominally experienced the same loading (because of the nearly symmetrical notches). When compared to the unbroken notch, the tissue at the corners of the fractured notch did not have as high of a residual stress. In these corner regions, the tissue appears to have elastically recovered after the notch fractured, resulting in a smaller residual stress in the mineral component. However, mineral stress can still be seen near the edges of the fracture where the tissue did not elastically recover. The reason is that we have made permanent changes to the matrix in this region and have broken or distorted collagen cross-links. Because the mineral is deposited in and around the matrix, the response of the mineral and matrix are coupled. In regions near the fracture, there are permanent changes to the matrix, but not necessarily permanent changes to the mineral. However, an increased stress in the mineral is observed because of the coupling with the permanently stressed matrix. If all the collagen was removed, the mineral might return to almost its original state. The average stresses near the beam 1 and 2 fracture edges were about 137 and 216 MPa (average of the two ROIs). Again, this was significantly higher than in control regions.

To determine the effects of protease inhibitor on bone spectra, protease inhibitor was added to the buffer used for all regions of beam 2, but not in the buffer used for beam 1. The protease inhibitor exhibited a band at 951 cm^{-1} that overlapped with the PO_4^{-3} v_1 band in bone. When the laser was focused on the bone surface, the 951-cm^{-1} band comprised approximately 1% of the total area of the PO_4^{-3} v_1 band, and

it was determined that the protease inhibitor did not interfere with CG calculations. However, in regions where the buffer was pooled (i.e., within the fracture), the spectrum of the protease inhibitor contributed approximately 20% or more to the total area. This contribution could not be effectively removed by subtraction. Multivariate techniques were not used to remove the contribution because of the continuous, overlapping distribution of protease inhibitor and bone. For these reasons, the data in the fractured region were not used and the regions were left as white space. The other small white spaces in Figs. 4(b) and 4(c) resulted from removal of data contaminated with a noise spike that overlapped with the PO_4^{-3} υ_1 band, or a fluorescent background that could not be properly removed by baselining.

Beam 3 displayed different stress patterns for both notches, and was significantly different from beams 1 and 2. The stress observed at both notches was less than that of beams 1 and 2. This lower-magnitude stress was spread out across the length of the notch and not really concentrated at the corners [Fig. 5(b)]. For the fractured notch, stress was present away from the edge of the fracture and across the middle of the image, suggesting the tissue did not relax during or after fracture, and the stress did not recover elastically. Another difference was that beam 3 fractured from the center of the notch, whereas the other specimens fractured at the corner of the notch where the greatest tension would be expected.

Differences among the specimens were analyzed to determine the reason for the discrepancy in residual stress patterns. Specimens 1, 2, and 3 were all excised from the dorsal-medial region of the Mc-3 bone of female thoroughbreds, from either the distal or proximal end of the bone. A mixture of left and right bones was used; however, previous studies have shown that no differences existed in collagen orientation[22] and bone mineral content (BMC)[23] for left and right bones. The most likely reason for the discrepancy in specimen stress response was the age of the specimens. Beam 3 came from a horse that was 6 years old, whereas beams 1 and 2 came from horses that were 2 and 4 years younger, respectively.

The average strength of equine Mc-3 bone peaks sometime between the age of 4 to 7 years; El Shorafa, Feaster, and Ott found that peak strength was attained within this range,[24] and Lawrence et al. showed that both BMC and bone breaking strength, defined as the maximum stress the material can withstand, peaked near 6 years of age.[23] From the force-displacement curves, the maximum breaking force for the 6-year-old bone (beam 3) was 54.9 N, whereas for the 2- and 4-year-old specimens it was 63.8 N and 66.5 N, respectively. In our study, the 6-year-old bone (specimen 3) was less strong than the younger bones. The study by Lawrence et al. also found that in maturing horses, the strength of bone was due mainly to the increasing BMC. The Raman mineral-to-matrix band ratio (intensity values of phosphate υ_1 at $\sim$959 cm^{-1}/proline at $\sim$853 cm^{-1}), a measure of the amount of mineral in bone, for the three specimens was calculated in the failed notch ROIs designated in Figs. 3(c), 4(c), and 5(c). The average mineral-to-matrix ratio for specimens 1, 2, and 3 were 13.9 ± 1.1, 13.8 ± 1.1, and 11.8 ± 1.6. The mineral-to-matrix ratio was lower in the beam that had the smallest breaking force. The lower mineral content, perhaps from recent remodeling, may have contributed to the lower strength

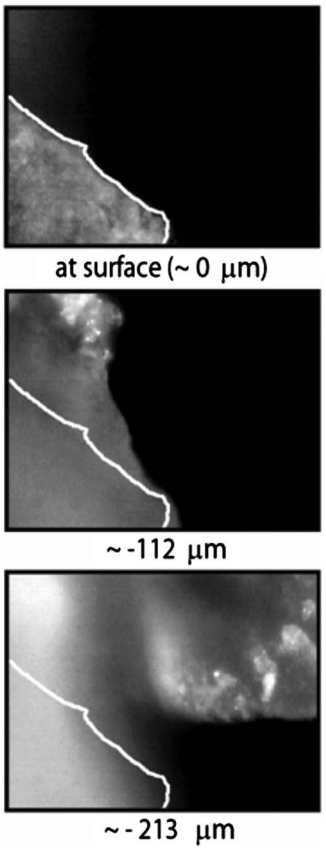

Fig. 7 Irregular fracture process. When bone fractured, the break was not perpendicular to the surface; regions of bone were present below the surface of the bone, as shown for specimen 3. The white outline corresponded to the uppermost surface of bone at the left edge of the fracture. The regions of bone below the surface contributed to the signal that was collected from within the fractured region.

of that beam. Another reason for the different stress patterns at both notches could be because the bone structure caused the stress distribution to be different than the two previous specimens. However, because of the small number of specimens, these conclusions are only preliminary.

It can be seen in Fig. 5(c) that signal was collected from within the fractured region. Unlike beam 2, no protease inhibitor was used for beam 3. The reason bone signal was collected was because the fracture process was irregular, and the break was not perpendicular to the surface. Regions of bone were present below the plane of best focus (i.e., plane of bone surface), as illustrated in Fig. 7. Because the Raman microprobe was not confocal, signal from these deeper layers was collected, albeit at a lower intensity.

In conclusion, residual stress in the loaded bone tissue was measured by analyzing band shifts in PO_4^{-3} υ_1. These mineral band shifts were a consequence of changes in spacing between phosphate cations and anions, which is a reversible effect. A band shift in the mineral component still could be measured after four-point bending, implying that the tissue near the unbroken notch and the edge of the fracture were left in a loaded state. Residual stresses in the strain and fail regions were significantly different than in control regions (0.0425 and 0.0169, respectively). In beams 1 and 2, the lo-

cation and pattern of the residual stresses was in agreement with that of the predicted stresses from a linear finite element analysis of the fracture specimen, where the highest stresses at the unbroken notch were concentrated at the corners. The calculated average stress magnitudes were lower than predicted, mainly because the dv/dP value used in the study was an estimate for equine bone, and the mineral distribution was not uniform. The exact stress distributions probably depend on specimen age, BMC, and local load distribution. Careful interpretation of Raman images was required because both multiple light scattering in bone and irregularity of the fracture site caused signal to be collected from below the uppermost surface of the bone (i.e., the best plane of focus).

Future work includes examining the stress response of the matrix. In fractured regions, collagen cross-links rupture, but the fate of cross-links just before bone breaks (i.e., region near unbroken notch) is not known, even though the breaking of cross-links is thought to be one of the last processes to occur before bone failure. Also, polarization measurements would be useful, because some mineral and matrix spectral bands are strongly polarized, and the orientation of different bone components could be determined.[25,26]

Acknowledgments

Dooley acknowledges support through NIH training grant T32 GM008353. Morris and Fyhrie acknowledge support through NIH grant R01 AR055222. We thank Kaiser Optical Systems for equipment support, Jacqueline Cole for help with statistical analysis, and Francis Esmonde-White for help with graphing applications.

References

1. J. Xu, D. F. R. Gilson, I. S. Butler, and I. Stangel, "Effect of high external pressures on the vibrational spectra of biomedical materials: Calcium hydroxyapatite and calcium fluoroapatite," *J. Biomed. Mater. Res.* **30**, 239–244 (1996).
2. S. N. Vaidya, C. Karunakaran, B. M. Pande, N. M. Gupta, R. K. Iyer, and S. B. Karweer, "Pressure-induced crystalline to amorphous transition in hydroxylapatite," *J. Mater. Sci.* **32**(12), 3213–3217 (1997).
3. J. Xu, D. F. R. Gilson, and I. S. Butler, "FT-Raman and high-pressure FT-infrared spectroscopic investigation of monocalcium phosphate monohydrate, $Ca(H_2PO_4)_2H_20$," *Spectrochim. Acta, Part A* **54**, 1869–1878 (1998).
4. J. Xu, I. S. Butler, and D. F. R. Gilson, "FT-Raman and high-pressure infrared spectroscopic studies of dicalcium phosphate dihydrate ($CaHPO_4 \cdot H_2O$) and anhydrous dicalcium phosphate ($CaHPO_4$)," *Spectrochim. Acta, Part A* **55**, 2801–2809 (1999).
5. P. Comodi, Y. Liu, P. F. Zanazzi, and M. Montagnoli, "Structural and vibrational behavior of fluorapatite with pressure. Part I. in situ single-crystal x-ray diffraction investigation," *Phys. Chem. Miner.* **28**, 219–224 (2001).
6. P. Comodi, Y. Lin, and M. L. Frezzotti, "Structural and vibrational behaviour of fluorapatite with pressure. Part II: in situ micro-Raman spectroscopic investigation," *Phys. Chem. Miner.* **28**, 225–231 (2001).
7. O. de Carmejane, M. D. Morris, M. K. Davis, L. Stixrude, M. Tecklenburg, R. M. Rajachar, and D. H. Kohn, "Bone chemical structure response to mechanical stress studied by high pressure Raman spectroscopy," *Calcif. Tissue Int.* **76**, 207–213 (2005).
8. P. Zhu, J. Xu, A. Ramamoorthy, D. H. Kohn, and M. D. Morris (unpublished).
9. J. A. Timlin, A. Carden, M. D. Morris, R. M. Rajachar, and D. H. Kohn, "Raman spectroscopic imaging markers for fatigue-related microdamage in bovine bone," *Anal. Chem.* **72**(10), 2229–2236 (2000).
10. M. D. Morris, A. Carden, R. M. Rajachar, and D. H. Kohn, "Effects of applied load on bone tissue as observed by Raman Spectroscopy," *Proc. SPIE* **4614**, 47–54 (2002).
11. A. Carden, R. M. Rajachar, M. D. Morris, and D. H. Kohn, "Ultrastructural changes accompanying the mechanical deformation of bone tissue: a Raman imaging study," *Calcif. Tissue Int.* **72**, 166–175 (2003).
12. G. Pezzotti and S. Sakakura, "Study of the toughening mechanisms in bone and biomimetic hydroxyapatite materials using Raman microprobe spectroscopy," *J. Biomed. Mater. Res.* **65A**, 229–236 (2003).
13. G. Pezzotti, "Introducing a unique measurement for biomaterial nanomechanics," *Key Eng. Mater.* **240–242**, 893–900 (2003).
14. G. Pezzotti, "Raman piezo-spectroscopic analysis of natural and synthetic biomaterials," *Anal. Bioanal. Chem.* **381**(3), 577–590 (2005).
15. M. D. Morris, W. F. Finney, R. M. Rajachar, and D. H. Kohn, "Bone tissue ultrastructural response to elastic deformation probed by Raman spectroscopy," *Faraday Discuss.* **126**, 159–168 (2004).
16. L. H. He, E. A. Carter, and M. V. Swain, "Characterization of nanoindentation-induced residual stresses in human enamel by Raman microspectroscopy," *Anal. Bioanal. Chem.* **389**, 1185–1192 (2007).
17. R. K. Nalla, J. H. Kinney, and R. O. Ritchie, "Mechanistic fracture criteria for the failure of human cortical bone," *Nature Mater.* **2**(3), 164–168 (2003).
18. C. A. Lieber and A. Mahadevan-Jansen, "Automated method for subtraction of fluorescence from biological Raman spectra," *Appl. Spectrosc.* **57**(11), 1363–1367 (2003).
19. V. Sergo, O. Sbaizero, and D. R. Clarke, "Mechanical and chemical consequences of the residual stresses in plasma sprayed hydroxyapatite coatings," *Biomaterials* **18**(6), 477–482 (1997).
20. G. Bigot, A. Bouzidi, C. Rumelhart, and W. Martin-Rosset, "Evolution during growth of the mechanical properties of the cortical bone in equine cannonbones," *Med. Eng. Phys.* **18**(1), 79–87 (1996).
21. T. Vo-Dinh, *Biomedical Photonics Handbook*, CRC Press, Boca Raton, FL (2003).
22. R. B. Martin, S. T. Lau, P. V. Mathews, V. A. Gibson, and S. M. Stover, "Collagen fiber organization is related to mechanical properties and remodeling in equine bone. A comparison of two methods," *J. Biomech.* **29**(12), 1515–1521 (1996).
23. L. A. Lawrence, E. A. Ott, G. J. Miller, P. W. Poulus, G. Piotrowski, and R. L. Asquith, "The mechanical properties of equine third metacarpals as affected by age," *J. Anim. Sci. (Savoy, Ill.)* **72**, 2617–2623 (1994).
24. W. M. El Shorafa, J. P. Feaster, and E. A. Ott, "Horse metacarpal bone: age, ash content, cortical area and failure stress interrelationships," *J. Anim. Sci. (Savoy, Ill.)* **49**, 979 (1979).
25. M. Kazanci, P. Roschger, E. P. Paschalis, K. Klaushofer, and P. Fratzl, "Bone osteonal tissues by Raman spectral mapping: Orientation-composition," *J. Struct. Biol.* **156**(3), 489–496 (2006).
26. M. Kazanci, H. D. Wagner, N. I. Manjubala, H. S. Gupta, E. Paschalis, P. Roschger, and P. Fratzl, "Raman imaging of two orthogonal planes within cortical bone," *Bone (N.Y.)* **41**(3), 456–461 (2007).